The Astrophysical Journal Supplement Series, 229:6 (9pp), 2017 March https://doi.org/10.3847/1538-4365/229/1/6

Morphological Properties of Slender Ca II H Fibrils Observed by SUNRISE II

R. Gafeira[1], A. Lagg[1], S. K. Solanki[1,2], S. Jafarzadeh[3], M. van Noort[1], P. Barthol[1], J. Blanco Rodríguez[4], J. C. del Toro Iniesta[5], A. Gandorfer[1], L. Gizon[1,6], J. Hirzberger[1], M. Knölker[7,9], D. Orozco Suárez[5], T. L. Riethmüller[1], and W. Schmidt[8]
[1] Max Planck Institute for Solar System Research, Justus-von-Liebig-Weg 3, D-37077 Göttingen, Germany; gafeira@mps.mpg.de
[2] School of Space Research, Kyung Hee University, Yongin, Gyeonggi 446-701, Republic of Korea
[3] Institute of Theoretical Astrophysics, University of Oslo, P.O. Box 1029 Blindern, NO-0315 Oslo, Norway
[4] Grupo de Astronomía y Ciencias del Espacio, University of Valencia, P.O. Box 22085, E-46980 Paterna, Valencia, Spain
[5] Instituto de Astrofísica de Andalucía (CSIC), Apartado de Correos 3004, E-18080 Granada, Spain
[6] Institut für Astrophysik, Georg-August-Universität Göttingen, Friedrich-Hund-Platz 1, D-37077 Göttingen, Germany
[7] High Altitude Observatory, National Center for Atmospheric Research, P.O. Box 3000, Boulder, CO 80307-3000, USA
[8] Kiepenheuer-Institut für Sonnenphysik, Schöneckstr. 6, D-79104 Freiburg, Germany
Received 2016 August 24; revised 2016 November 14; accepted 2016 November 30; published 2017 March 22

Abstract

We use seeing-free high spatial resolution Ca II H data obtained by the SUNRISE observatory to determine properties of slender fibrils in the lower solar chromosphere. In this work we use intensity images taken with the SUFI instrument in the Ca II H line during the second scientific flight of the SUNRISE observatory to identify and track elongated bright structures. After identification, we analyze theses structures to extract their morphological properties. We identify 598 slender Ca II H fibrils (SCFs) with an average width of around 180 km, length between 500 and 4000 km, average lifetime of ≈400 s, and average curvature of 0.002 arcsec^{-1}. The maximum lifetime of the SCFs within our time series of 57 minutes is ≈2000 s. We discuss similarities and differences of the SCFs with other small-scale, chromospheric structures such as spicules of type I and II, or Ca II K fibrils.

Key words: Sun: chromosphere – Sun: magnetic fields – techniques: imaging spectroscopy

Supporting material: animation

1. Introduction

Large parts of the solar surface are littered with small-scale fibrils, loops, and jets, connecting the photosphere to the chromospheric layers. These structures, seen in radiation, are thought to follow magnetic field lines (e.g., Jafarzadeh et al. 2017b) anchored in photospheric magnetic flux concentrations, or in the weaker internetwork elements (Wiegelmann et al. 2010). Except for regions with large magnetic flux concentrations, such as sunspots or large pores, these structures play an important role in transporting the energy from the solar surface to the chromosphere and to the corona, either as a channel for the propagation of waves (e.g., van Ballegooijen et al. 2011), or as the location for small-scale reconnection events (Gold 1964; Parker 1972). Observations in the Ca II H and K lines at high spatial resolution (e.g., from the Swedish Solar Telescope, SST, Pietarila et al. 2009), and under seeing-free, stable conditions using the *Hinode* space observatory, shed new light on these small-scale structures, e.g., leading to the discovery of a new type of spicule (type-II, de Pontieu et al. 2007; Pereira et al. 2012).

The unique observational conditions provided by the SUNRISE balloon-borne solar observatory (Barthol et al. 2011; Solanki et al. 2016) allow us to observe the solar chromosphere in the core of Ca II H at constantly high temporal and spatial resolution, without the influence of seeing. This has given us the possibility to look at the structures present in the lower chromosphere at a level of detail not achieved before. Of special interest in this work are the so-called slender Ca II H fibrils (SCFs): similar to spicules or chromospheric jets, these ubiquitous features outline the magnetic field in the lower chromosphere and offer the possibility of gaining insight into the physical processes in this layer of the solar atmosphere (Pietarila et al. 2009; Wöger et al. 2009; Jafarzadeh et al. 2017c).

In this work, we develop a technique for the automatic detection of SCFs (Section 3) enabling us to investigate their statistical properties. We discuss the lifetime, width, length, curvature, and temporal evolution of brightenings within the individual SCFs (Section 4), and compare these morphological properties to similar, small-scale structures observed with *Hinode* and the SST (Section 5).

2. Data

The observations on which this study is based were taken by the SUNRISE balloon-borne solar observatory (Solanki et al. 2010; Barthol et al. 2011; Berkefeld et al. 2011; Gandorfer et al. 2011; Martínez Pillet et al. 2011) during its second science flight (Solanki et al. 2016) in 2013 June, referred to as SUNRISE II. The data set used was recorded from 2013 June 12 at 23:39 UT to 2013 June 13 at 00:38 UT, and covers part of the active region NOAA 11768 including most of the following polarity, the polarity inversion line, and also an emerging flux region lying between the two opposite polarity regions. At the time it was observed the active region was still young and developing and was located at $\mu = \cos\theta = 0.93$, where θ is the heliocentric angle. The heliocentric coordinates of the center of the SUNRISE Filter Imager (SUFI) field-of-view (FOV) were $x = 508''$, $y = -274''$. The one hour long time series is composed of a total of 490 images taken using the SUFI (Gandorfer et al. 2011) in three wavelength bands, the Ca II H 3968 Å line using a narrow-brand filter with a full width at half maximum (FWHM) of 1.1 Å. The integration time of each image was 500 ms. A broader Ca II H channel with a FWHM of

[9] The National Center for Atmospheric Research is sponsored by the National Science Foundation.

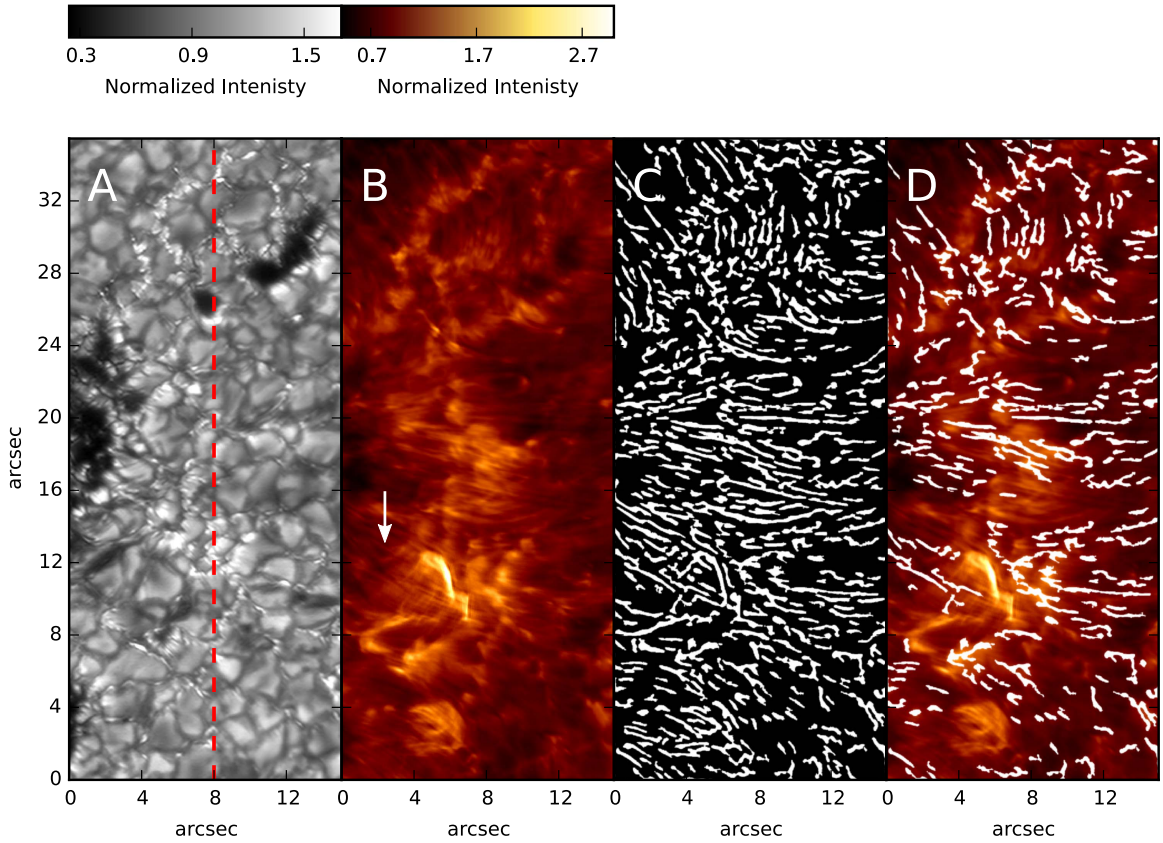

Figure 1. (A) Continuum image recorded on 2013 June 13 at 00:31 with the 3000 Å continuum filter, (B) cotemporal, coaligned Ca II H image, (C) binary mask resulting from the fibril identification method, and (D) superposition of the Ca II H image and the identified fibrils. The dashed red line on image A indicates the position of the slit used in Figure 4. The white arrow on image B points to a sample fibril that is shown in greater detail in Figure 2.

(An animation of this figure is available.)

1.8 Å recorded images with an integration time of 100 ms, and a broad-band channel centered on 3000 Å, with a FWHM of 50 Å, delivered continuum images with an integration time of 500 ms. The data were reconstructed using the multi-frame blind deconvolution (MFBD, van Noort et al. 2005) technique to account for the image degradation by the telescope. After the MFBD reconstruction, the data had a spatial resolution close to the diffraction limit of the SUNRISE telescope, which is at the wavelength of the Ca II H line, approximately 70 km. The cadence (i.e., the time between two consecutive images at the same wavelength) was 7 s. The data set, the data reduction, and reconstruction are described in detail by Solanki et al. (2016).

3. Fibril Detection and Tracking

The main goal of this work is to determine the basic morphological properties of the SCFs. To this end we must first identify and track the bright elongated structures that can be seen in Figure 1(B). To perform this identification we apply a series of image processing and contrast enhancement techniques. We start by subtracting a boxcar-averaged version of the original image from itself to remove the low frequencies and to enhance the structure with the typical dimensions of the fibrils. The size of the boxcar window is set to 20 pixels, corresponding to approximately 0.″4. Then, we apply a sharpening filter using the UNSHARP_MASK function from the Interactive Data Language (IDL, Exelis Visual Information Solutions, Boulder, CO) to increase the global image contrast. This unsharp mask involves the following steps: (i) the original image is smoothed with a Gaussian filter having a width of 10 pixels; (ii) this smoothed image is then subtracted from the original image; and (iii) the resulting difference image is again added to the original image. In a next step, an adaptive histogram equalization is performed, described in detail by Pizer et al. (1987), again using the implementation in IDL (version 8.3) with the standard parameter settings to further increase the contrast. Finally, we apply a boxcar smoothing with a width of 3 pixels to remove frequencies beyond the spatial resolution of SUNRISE, introduced by the steps described above.

The resulting contrast-enhanced images highlight most of the fibrils very well and allow the application of a binary mask with a threshold of 50% of its maximum intensity, separating the fibrils from their surroundings. The same threshold was used for the entire FOV of SUFI and for all frames in the time series, ensuring an unbiased determination of the length, width and shape of the identified fibrils.

Finally, we exclude all detected regions smaller than 200 pixels in area (corresponding to $\approx$0.1 arcsec^2), which is approximately the area of a circle corresponding to a spatial resolution element close to the diffraction limit. An example of such a binary mask resulting from this process is shown in Figure 1(C).

The next step is to track individual fibrils in time to analyze their evolution. For this task we take six consecutive frames and identify those regions where the binary mask marks the presence of a fibril in at least 10 pixels at the same image position in at least five out of a total of six consecutive frames. After this, we

assign each fibril a tracking index. Then we advance one frame and repeat the same analysis, checking whether each newly identified fibril already has a tracking index. If so, it is counted as the temporal continuation of the fibril from the previous frame; if not, it is counted as a new fibril.

This method ensures, with a high level of confidence, that we catch the temporal evolution of individual fibrils. The method works very well for nicely separated fibrils, but it has some limitations in two special cases: (i) if a significant number of other fibrils cross the identified fibril, the binary mask will show either interruptions or the crossing fibrils are counted toward the identified fibril, and (ii) if the identified fibril has a high transverse velocity (i.e., perpendicular to the fibril axis), it will move out of the detection window in the next frame.

The latter effect is particularly important in the regions of magnetic flux emergence (near $x = 12''$, $y = 9''$) where the fibrils are much more dynamic than in the rest of the SUFI FOV.

Due to the large density of fibrils, about 80% of those detected suffer from the presence of crossing or very close neighboring fibrils. The identified fibril and those crossing it are often misidentified as a single structure with a complex, frayed shape instead of the expected linear, elongated one identified by the white arrow in Figure 1. If such a complex shape does exist over several consecutive frames, a correct fibril identification using a binary mask is nearly impossible.

To address this problem we introduce the concept of a fibril's reference backbone, which we define as the second-order polynomial best fitting the long axis of the fibril and therefore marking the ridge of maximum brightness. It is computed by first reducing the fibril in every frame of the time series of Ca II H images to a shape that is a single pixel in width. Each such pixel is equidistant from the fibril's lateral boundaries (which are the locations where the brightness drops below the threshold). The set of all such (single) pixels constitute the fibril's backbone. Afterwards, the fibrils of the individual frames are fitted with a second-order polynomial. This polynomial is extended by the average width of this fibril (see Section 4.2), on both end points of the fibril to compensate for the shortening due to the reduction of the fibril to a single pixel line. The resulting curve we define as the reference backbone. Fibrils of complex shape, often produced by intersecting fibrils or by not well separated fibrils, are usually poorly fitted (χ^2 values are higher than 6), and are excluded from this averaging. An example of this process is illustrated in Figure 2, where we show one identified fibril and its temporal evolution (left panels) and the overplotted fibril backbone (black line, right panels). The gray shaded area around the skeleton displays the width of the fibril, computed in every single frame using the method described in Section 4.2.

The fibril is well identified in all six plotted time steps. However, its length may well be underestimated, as the detection method often fails to follow the fibril to its very end, as can be seen by eye. Fibrils often become too faint near their ends to be reliably identified by our method. Being faint, they are also susceptible to interference from background structure and crossings by other fibrils. We have therefore not attempted to extend the lengths of the individual fibrils. Instead, we consider that the fibrils that we have identified are often in fact fibril fragments (see Pietarila et al. 2009), i.e., parts of longer fibrils. For brevity we will continue to call them fibrils (or SCFs) in the following, although in many cases we may be discussing only parts of the full fibrils.

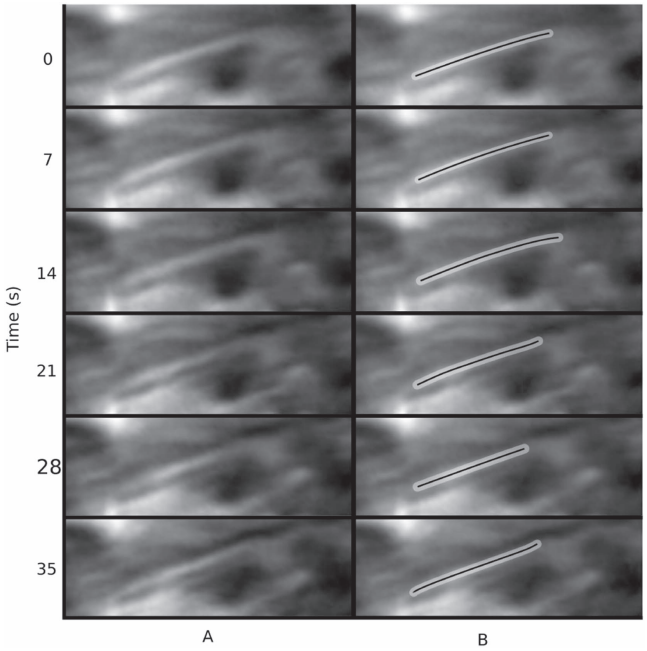

Figure 2. Example of the temporal evolution of a tracked fibril. The left panels show the original Ca II H images, representing the temporal evolution of a fibril identified over a set of six consecutive SUFI frames. The right panels show the same images, overplotted with the result of the detection and tracking method described in the main text. The black lines represent the individual backbones and the gray regions indicate the width of the fibril computed using the method explained in Section 4.2.

We obtain a total of 598 fibrils in the SUFI FOV over the entire time series. One snapshot with the identified fibrils overlayed on top of the corresponding Ca II H image is presented in panel D of Figure 1.

4. Fibril Morphology

The result of the fibril tracking allows for a statistical analysis of the SCFs and allows computing of several of their morphological properties. In this section we present the results obtained for lifetime, length, width, and curvature of SCFs extracted using information obtained from the detection and tracking methods.

4.1. Lifetime

Visual inspection of the movie created from the time series of SUFI images (see online material, `sufi.mp4`) reveals the highly dynamical nature of the SCFs. The identification of the individual fibrils over multiple time steps allows us to produce a lifetime histogram with a lower limit of 35 s (corresponding to five consecutive frames, which is the minimum length of time we require for a fibril to survive to be identified as such) and an upper limit given by the length of the time series (57 minutes). Only fibrils with a defined start- and end-time are included in the histogram, i.e., fibrils that are observed in the first or the last frame of the series are excluded from this analysis.

This lifetime histogram is presented in Figure 3 (all histograms shown in this paper are normalized so that they have a total area equal to 1). It shows a clear exponential decay with increasing lifetime at a decay rate of 2.5×10^{-2} s^{-1} (red

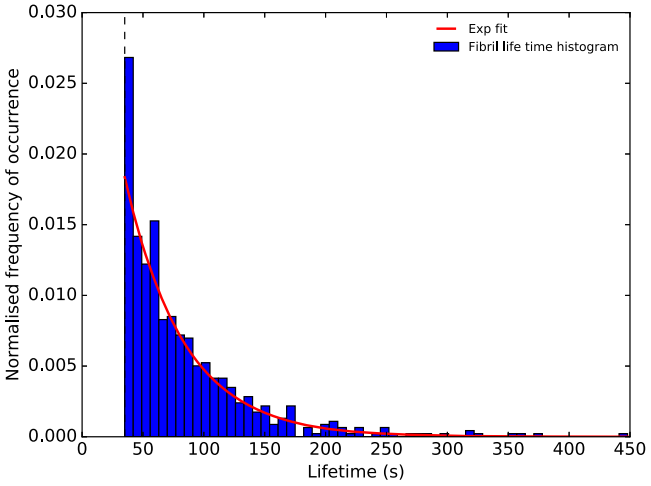

Figure 3. Fibril lifetime distribution and an exponential fit to the observed distribution (red line). Plotted is the frequency of occurrence of fibrils per lifetime bin vs. the lifetime. Only fibrils with a minimum lifetime of 35 s are included.

line). About 80.3% of the fibrils have lifetimes between 35 s (i.e., the lower threshold) and 100 s, and only 1.6% live longer than 300 s (see also Table 1). It must be noted that these lifetimes are likely underestimated for multiple reasons. By considering only fibrils that are born and die in the course of the observed time series, we bias the histogram toward shorter-lived fibrils due to the finite length of the time series. Changes in either the fibril or its background or neighboring fibrils can also cause its lifetime to be underestimated. Changes in the brightness or position of the fibril can cause the tracking algorithm to lose it, thus curtailing its apparent lifetime. Similarly, variations in the overall brightness and/or quality of the image may cause an apparent disappearance and reappearance of the same fibril, which is then counted as two individual fibrils, both with a shorter apparent lifetime. In addition, fibrils clearly visible on the dark background of the outer parts of the pore and its immediate surroundings become hard to follow above the bright magnetic concentrations in the right part of the image. Also, there appear to be weak, short, and strongly inclined fibrils connecting bipolar regions in the right part of the figure that are directed from the NE to the SW, which cross the longer mainly E–W directed fibrils. Similarly, in the upper half of the figure, fibrils emanating from the large pore often cross other fibrils pointing in different directions. Hence the automated identification catches only individual relatively undisturbed fragments of fibrils.

To investigate this effect, introduced by the tracking method, we analyzed the position of the fibrils in a spacetime diagram. Figure 4 shows the temporal evolution of fibrils along an artificial slit at a fixed x-position, $x = 8''$, indicated by the red, dashed line in Figure 1(A). The slit stays fixed at this position throughout the whole time series. Plotted is a binary mask, with the presence of (identified) fibrils indicated in blue. In many cases, the blue patches look like an intermittent, nearly horizontal line, indicating that this particular fibril first disappears and then reappears at almost the same location. For better visibility, one such intermittent line is highlighted in red. Most of the longer interruptions indicate a true darkening (or complete disappearance) of the fibril, with a later reappearance within the same magnetic flux tube or set of field lines, which obviously has a lifetime longer than the fibril itself. Also, some of the brightness variations leading to interruptions of fibrils in a spacetime plot may be related to the sausage-mode waves identified in the fibrils by Gafeira et al. (2017).

To identify the intermittent fibrils, exemplified by the one marked in red in the spacetime diagram presented in Figure 4, we use exactly the same approach as described in Section 3, but with different parameter settings, allowing us to bridge the longer temporal gaps. In Section 3, we required that 10 common pixels must exist in at least five out of six consecutive frames, to ensure that we are really tracing the same fibril. Here, we relax this condition and require that 10 common pixels must exist in only two out of 16 frames. This closes most of the temporal gaps visible in Figure 4, at the expense of an increased likelihood of catching another fibril, which moved into the same position as the previous fibril within $\leqslant$105 s (15 frames).

The so-determined lifetime is still underestimated due to the maximum allowed gap length of 15 frames, and the finite length of the time series, as longer-lived fibrils are more likely excluded because they were alive either at the beginning or the end of the time series. The latter effect can be corrected following Danilovic et al. (2010a): we multiply the frequency of occurrence of fibrils that live for m frames by the factor $(n-2)/(n-1-m)$, where n is the total number of frames in the time series. This correction has been taken into account in Figure 5. The average lifetime of the fibrils obtained after all these corrections is Figure 5 is 446 s. Other parameters describing the lifetime distribution are listed in Table 1.

We then compared this lifetime distribution with that from the automatic tracking method. The new distribution, presented in Figure 5, now shows a maximum at a lifetime of $\approx$150–300 s. More than 58% of the fibrils have lifetimes longer than 300 s; 8.5% even live longer than 15 minutes. The red line indicates an exponential fit to the tail of the distribution (i.e., to the distribution of lifetimes longer than 400 s) and the green line indicates a log-normal fit to the entire distribution. The decay rate is now found to be $3.0 \times 10^{-3}\,\mathrm{s}^{-1}$, meaning that the distribution drops off nearly an order of magnitude slower than before the correction of the lifetimes for the intermittency. Obviously, the magnetic structure (possibly some kind of flux tube) housing the SCFs is considerably longer-lived than the brightenings in the Ca II H line. It could also be that the source of the brightening (located, e.g., in the photosphere) is intermittent, causing a bright fibril to appear equally intermittently.

4.2. Width

The automatic detection method delivering the backbone of the fibrils facilitates the computation of the widths of the SCFs. This computation, illustrated in Figure 6, is done by first selecting the position of the maximum intensity of a fibril along a virtual slit, with a length of $0\farcs6$, oriented perpendicularly to the backbone of the fibril and placed at the center of the fibril's backbone. Then we fit a weighted Gaussian function plus a linear background to the intensity on the slit. Points closer to the maximum intensity are given larger weights, in order to avoid that the fit is negatively influenced by close neighboring fibrils. We then take the FWHM of the Gaussian as a measure of the fibril's width. To further minimize the influence of neighboring or intersecting fibrils we require the side flanks of the fibril to be clearly

Table 1
Summary of the Morphological Properties of the SCFs

Parameter	Lifetime (excl. gaps)	Lifetime (incl. gaps)	Length	Width	Curvature
Functional form	exponential	log-normal	log-normal	Gaussian	symmetric
Range	35–450 s	35–2000 s	500–4500 km	100–270 km	-0.04–0.04 arcsec^{-1}
Mean value	n/a	446 s	1380 km	182 km	0.002 arcsec^{-1}
Standard deviation	n/a	310.27	760 km	34 km	0.019
Skewness	n/a	3.70	2.51	n/a	2.26
Kurtosis	n/a	31.60	3.24	n/a	17.83
Exp. decay rate	25 (ms)$^{-1}$	3.0 (ms)$^{-1}$	n/a	n/a	n/a

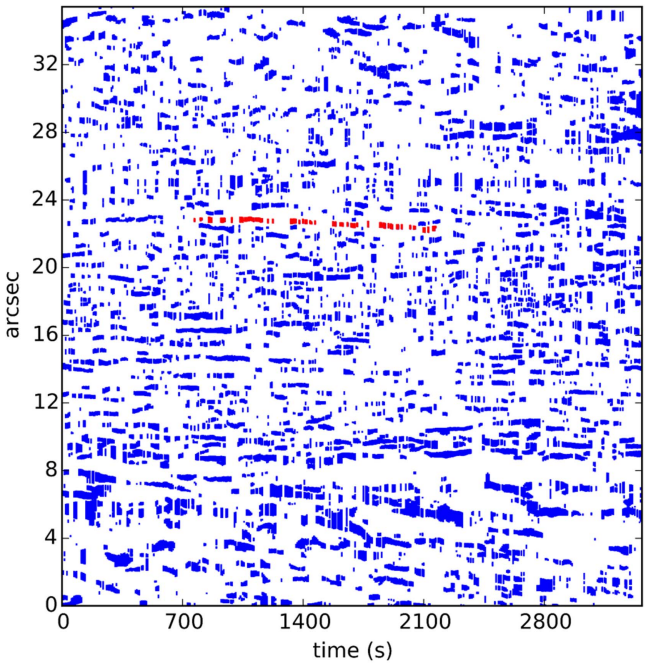

Figure 4. Space–time diagram of the presence of fibrils along an artificial slit indicated by the red dashed line in Figure 1(A). One fibril is marked in red to exemplify its intermittent appearance.

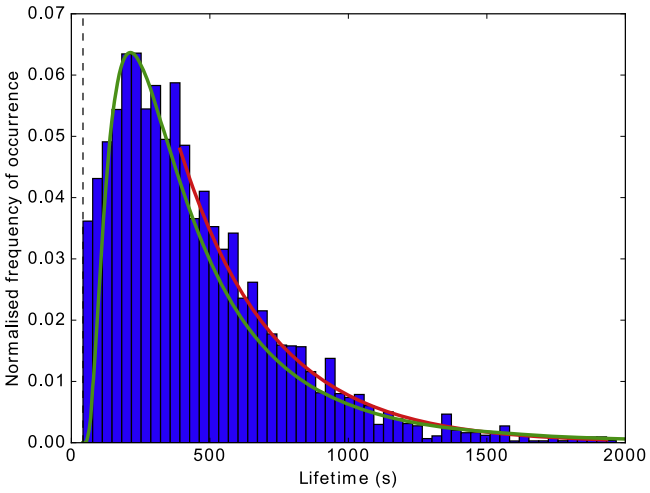

Figure 5. Fibril lifetime distribution taking into account the intermittency of the detected fibrils. The red line indicates an exponential fit for fibrils with a lifetime $\geqslant$400 s. The green line indicates the respective log-normal fit.

visible and the linear background brightness variation to have a slope smaller than 0.002 per km in units of the normalized intensity.

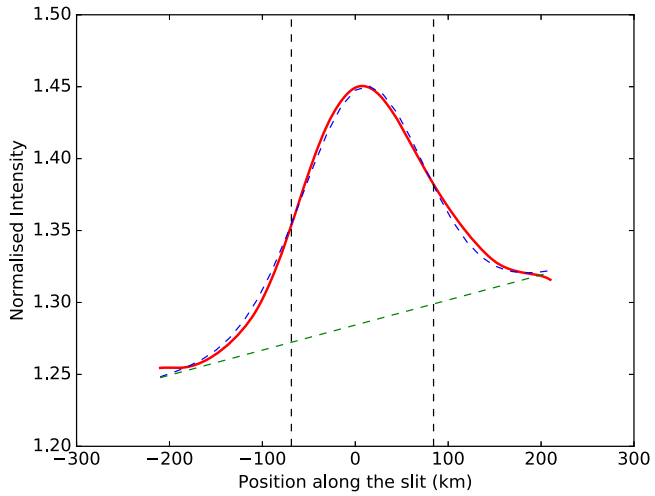

Figure 6. Example for the determination of the fibril width by fitting a superposition of a Gaussian and a linear function (dashed blue line) to the brightness variation (red line) perpendicular to the fibril backbone. The linear function (dashed green line) takes into account the variation of the background brightness. The width of the fibril, indicated by the vertical dashed lines, is the FWHM of the Gaussian.

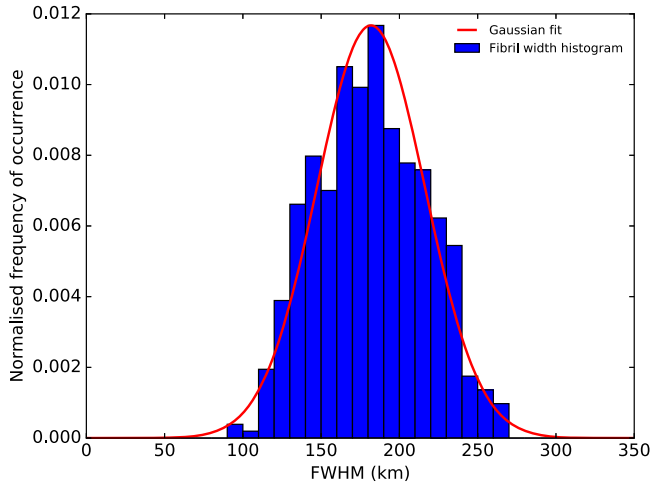

Figure 7. Width distribution for each individual fibril detected in all the frames and its respective Gaussian fit (red curve).

The above procedure is repeated for all fibrils in each frame to produce the histogram presented in Figure 7. This distribution of fibril widths is reasonably well represented by a Gaussian function (red line) with a mean width of $\approx$182 km (see Table 1 for the other fit parameters of this Gaussian). The narrowest fibril was determined to have a width slightly smaller than 100 km, which is above the spatial resolution of SUNRISE of around 70 km at the wavelength of Ca II H. This fact might

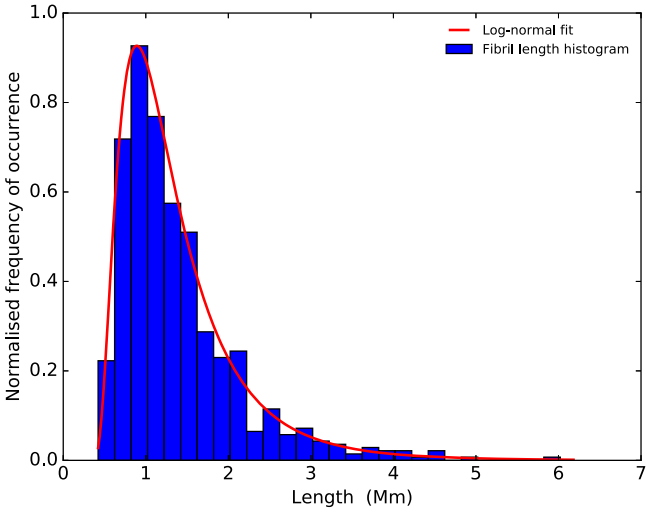

Figure 8. Distribution of the backbone length, averaged over the lifetime of the SCFs (blue), and respective log-normal fit (red curve).

suggest that ≈100 km is a lower limit for the width of solar fibrils, and that SUNRISE is actually resolving the fibrils. However, we are aware of the fact that the determination of the fibril width is not without problems. The fibrils have to be identified against a relatively bright photospheric background contamination resulting from the broad transmission profile of the Ca II H filter used in SUFI. Additionally, the width determination method, based on the fitting of a Gaussian function, is likely to smear out structures at the diffraction limit of the telescope, resulting in a larger minimum width.

The study of the width of Ca II K fibrils by Pietarila et al. (2009) showed minimum fibril widths of only 70 km, corresponding to the diffraction limit of the SST. Their analysis method was based on a binary mask, which is possibly better suited to determining the minimum widths of the fibrils, but has disadvantages in properly characterizing broader fibrils. When applying our technique to a sample of the fibrils in the data set used by Pietarila et al., we also get ≈100 km for the minimum width of their Ca II K fibrils, in accordance with our SUNRISE/SUFI measurements. We therefore conclude that the minimum width of our Ca II fibrils is likely to be set by the spatial resolution of the SUNRISE telescope.

4.3. Length

An important parameter returned by the automatic tracking method is the length of the detected SCFs, which we define as the length of the reference backbone as described in Section 3, plus the average of the widths computed in Section 4.2 at both end points. This addition is necessary to compensate for the effect when reducing the fibril to the single-pixel backbone, which reduces the backbone length on both ends approximately by the width of the fibril. The length of the fibril as determined here would correspond to the distance from end-to-end of the shaded area in each of the right-hand panels of Figure 2. Fibrils at the edge of the FOV are excluded from the analysis.

The histogram in Figure 8 shows that the detected fibrils are rather short, with a minimum length of ≈500 km. The mean length of the fibrils is ≈1300 km, and we could not find any fibril longer than 4500 km. The length distribution nicely follows a log-normal distribution, indicated by the red line in Figure 8 (for the fit parameters see Table 1).

Just as with the longer-lived fibrils, the longer fibrils are also more likely to be excluded because they touch one of the boundaries of the FOV. We again follow Danilovic et al. (2010a) and multiply the frequency of occurrence of fibrils that have a length of m pixels by the factor $(n-2)/(n-1-m)$, where n is the distance from one edge of the frame to the other in the average direction of the fibril. This correction has been taken into account in Figure 8. The average length of the fibrils is found to be 1.38 Mm. It is worth noting that their length does not correlate very well with their lifetime (the correlation coefficient is only 0.3).

The short length of the fibrils may be an artifact of the automated identification technique, so that we are looking at fragments of fibrils in many cases (see the discussion in Pietarila et al. 2009, and in Section 3). In the blow-up of the central section of the Ca II H image plotted in Figure 1(B) (data after MFBD reconstruction) many long fibrils are seen, some of them reaching 10″ in length. However, these long fibrils are often interrupted, or cut by other structures, making it hard for our simple identification algorithm to recognize them as a single long entity. Instead, the identification procedure breaks them into shorter fibrils.

There is also a general geometrical separation between the longer and shorter fibrils, at least as seen by eye, in the sense that the longer fibrils are found more in the central-lower part of Figure 1(B) directed roughly E–W, while the shorter fibrils are located in the upper part of the figure, in particular surrounding the small pores. In addition, the pattern of seemingly very short fibrils, or rather small bright patches in the lower left part of the image, may be produced by crisscrossing longer fibrils.

4.4. Curvature

The reference backbone of most of the fibrils can be fitted nicely with a second-order polynomial. This has partly to do with the fact that the automatically identified fibrils are rather short, but also because the fibrils are expected to outline loop-like magnetic flux tubes (although rather flat ones; see Jafarzadeh et al. 2017a; Wiegelmann et al. 2016): the slanted view at a heliocentric angle of $\theta \approx 22^\circ$ makes loop-like structures appear similar to parabolas.

We define the curvature, κ, of a fibril as the reciprocal value of the radius of the largest circle fitting the fibril tangentially, i.e., the so-called osculating circle. For a second-order polynomial, κ is defined as $2a$, where a is the second-order polynomial coefficient. The histogram in Figure 9 shows the curvature distribution obtained from all reference backbones of the time series. The distribution is nearly symmetric with a slight offset toward a positive curvature, with a mean value of 0.002 arcsec^{-1}.

4.5. Brightness Variation

The definition of a fibril backbone simplifies not only the study of the morphological properties discussed in the previous section, it also allows us to visualize the temporal evolution of intensity fluctuations within the fibril itself. This is achieved by putting an artificial mesh onto the reference backbone of the fibril, with the grid lines being parallel and perpendicular to the backbone. The perpendicular grid lines cover a region of ±0.″3 around the backbone; the parallel grid lines have the same length and curvature as the backbone itself. More information

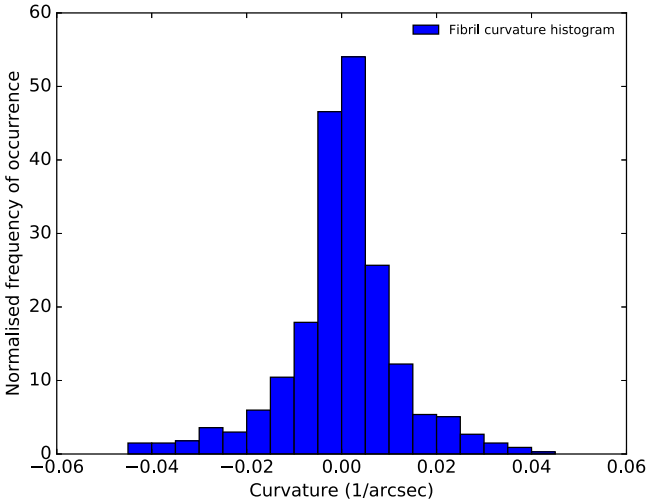

Figure 9. Curvature distribution of the fibril's reference backbones.

on the mesh and gridlines, including an illustration, can be found in Gafeira et al. (2017).

This mesh allows us to straighten the fibril by interpolating the brightness of the original image to the grid points of the mesh. Since the mesh was defined on the reference backbone of the fibril, we can now nicely follow the temporal brightness variation within the individual fibrils in plots such as the examples presented in Figures 10 and 11. These two plots show two different types of brightness variation and propagation along the fibril backbones. In Figure 10 the intensity decreases from the center to the endpoints, whereas in Figure 11 the intensity decreases from the endpoints of the fibril to its center. After visual inspection of all fibrils we find that the first type is the more common (around 54% of the the fibrils are of this type), and the second type is observed in ≈25% of the fibrils. For the remaining ≈21% it is difficult to clearly categorize the distribution of the brightness along the fibril axis, with only a very small fraction of those showing a brightening at one endpoint only. We could not find any obvious correlation between the type of the brightening (central or endpoint) with other parameters of the fibrils (length, width, absolute value, lifetime). It can also be seen that the width of the fibrils is not constant along the the length of the fibril. In general, the fibrils are broader at the locations where they are also brighter.

Note that in some cases, a fibril changes from having its brightness peak at its center to having it near its ends. Obviously, the brightness of the fibril varies with time, as can be seen in Figures 10 and 11. Gafeira et al. (2017) have pointed out that these variations are often periodic and occur mainly in (anti-)phase with oscillations in the width of the fibril. They identified these variations with sausage-mode waves.

5. Discussion and Conclusions

In this paper we present a first quantitative study of the morphological properties of SCFs aimed at measuring their parameters, such as lifetime, length, width, curvature, and brightness structure. We apply an automatic fibril detection algorithm based on several unsharp masking steps to identify the backbone of the fibrils (i.e., the curve following the central brightness ridge along the long-axis of the SCF). This allows us to identify, measure properties of, and perform a statistical analysis on 598 SCFs. We obtain values for the lifetime between

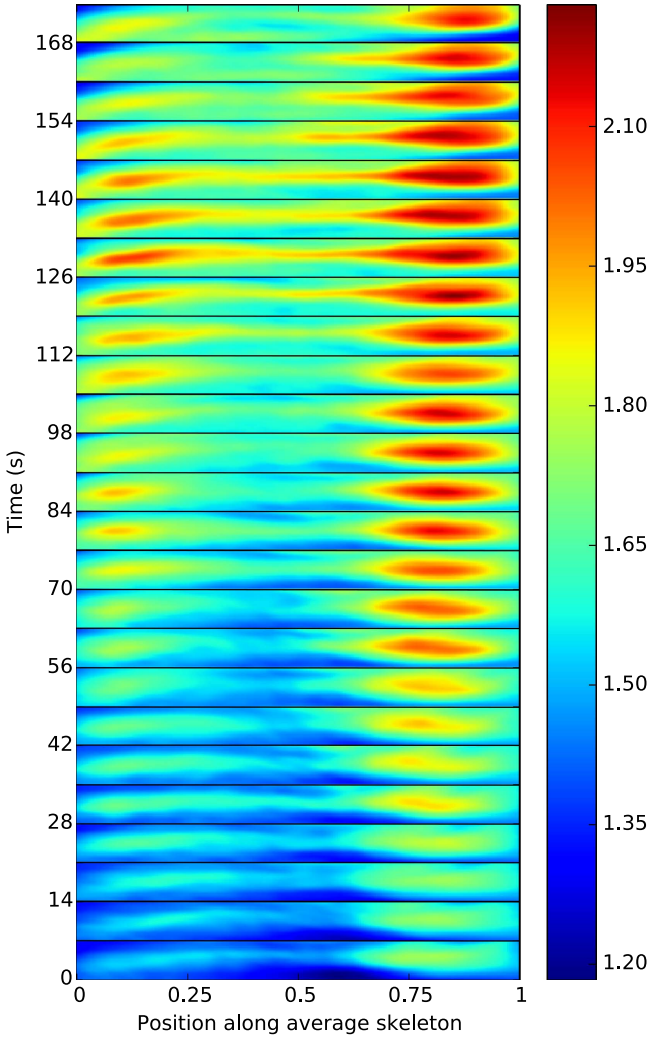

Figure 10. Temporal evolution of a SCF with a central brightening. The stacked images show the straightened fibril, with the backbone parallel to the x-axis in the center of each bin, surrounded by a $\pm 0\farcs3$ wide area covering the fibril. The individual images, recorded every 7 s, are separated by horizontal black lines. The length of the reference backbone of this fibril is 1620 km.

half a minute and half an hour (when taking into account the intermittency in fibril visibility), lengths between 0.5 and 4.5 Mm, and widths between 100 and 270 km. The fibrils show a wide distribution of curvatures, with a slight preference for a positive curvature, in agreement with the expected curvatures of low-lying loops observed at a position away from the solar disk center. We also identify two different morphologies of the evolution of the brightness within individual fibrils. In one type the intensity increases starting from the center and moving to the edges, while in the other type the increase in intensity first becomes visible near one or both of the ends and expands from there toward the center of the fibril.

Intersecting fibrils and not well separated fibrils cause problems in the automatic tracking of them, mainly leading to a failure in detecting fibrils longer than 4.5 Mm, although visual inspection of the SUFI Ca II H images shows that such fibrils do exist. The contrast between the measured short lengths and the pattern of extended fibrils in parts of the SUFI FOV suggests that the automated technique is identifying relatively undisturbed parts of fibrils as whole fibrils. Between these undisturbed fragments a given long fibril may be intersected by other fibrils,

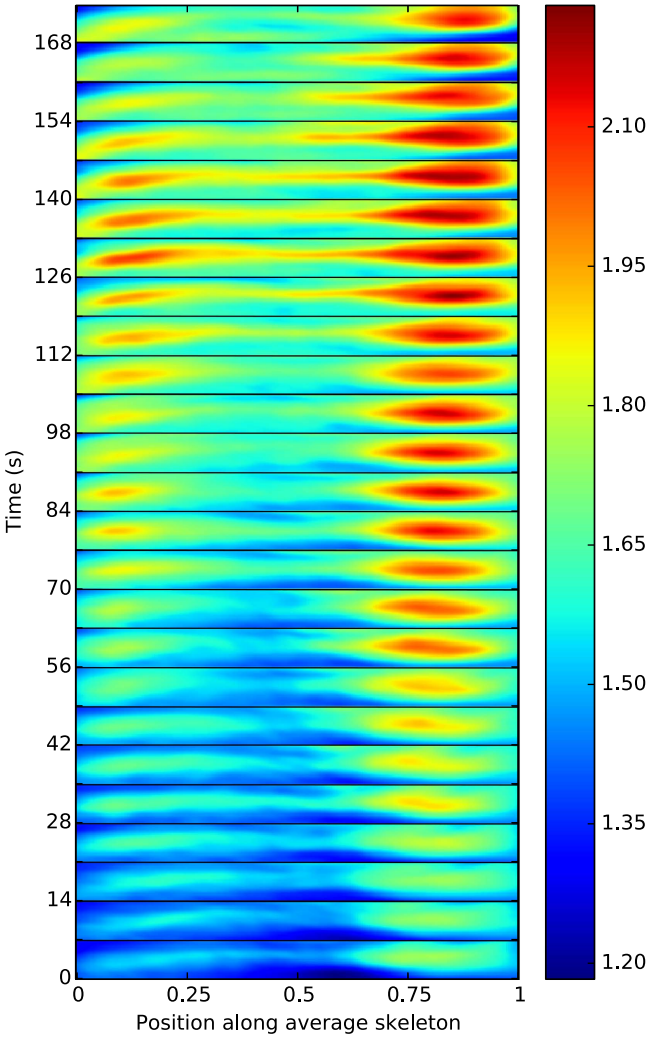

Figure 11. Same as Figure 10 for a SCF with endpoint brightening. The length of the reference backbone of this fibril is 2800 km.

or disturbed by underlying bright points, reversed granulation, and acoustic grains. This complex picture may arise because at the height of the SCFs, the Ca II H line may not be entirely optically thick, so that radiation from below can pass through possibly multiple layers of fibrils. This may have to do with the 1.1 Å FWHM of the filter employed by SUFI, which includes not just the H_2 and H_3 features of the line core, but also parts of the inner wings. The H_2 and H_3 features sample the lower to middle chromosphere, while the inner wings are mainly sensitive to the upper photosphere (see the heights of formation computed by Danilovic et al. 2014 and, Jafarzadeh et al. 2017a, 2017b).

The results of the present analysis allow us to relate SCFs to small-scale elongated, chromospheric structures already known from the literature. In Table 2 we list the properties of the SCFs together with those of type I and type II spicules (from Pereira et al. 2012), and of Ca II K fibrils (as deduce by Pietarila et al. 2009). Spicules show considerable similarities to the SCFs with regard to the range of widths (although the Ca fibrils studied by us and, in particular, those by Pietarila et al. are on average narrower).

The difference in width between the fibrils seen by Pietarila et al. in Ca II K and those studied by us in Ca II H is puzzling. It has at least partly to do with the difference in technique, as the application of our technique to a sample of fibrils identified by

Table 2
Comparison of Some Morphological Properties between SCFs Observed in Ca II H and in and Ca II K Spicules

	Lifetime	Width	Length
SCFs (this work)	35–450 s (35–2000 s)[a]	100–500 km	0.5–4.5 Mm
mean value	80 s	182 km	1.38 Mm
Type I spicules[b]	150–400 s	100–700 km	4–8 Mm
mean value	262 s	348 km	6.87 Mm
Type II spicules[b]	50–150 s	100–700 km	3–9 Mm
mean value	165 s	319 km	7.75 Mm
Ca II K[c]		75–150 km	
mean value		100 km	≈0.9 Mm

Notes.
[a] After taking into account the intermittent fibrils, see Section 4.1.
[b] Pereira et al. (2012).
[c] Pietarila et al. (2009).

Pietarila et al. (2009) returns larger widths than those found by those authors. Other factors may also contribute to the difference in width. Thus, it may have to do with different optical thicknesses, or that our observations were recorded in a larger, more intensely active region.

Both types of known spicules are considerably longer than our SCFs, with even the shortest spicules being close to the longest SCFs that we find. This difference in length may be a selection effect, however, as only the longer spicules are clearly identified at the limb, whereas shorter ones are buried in the forest of features at the solar limb. Conversely, our technique most likely underestimates the lengths of the fibrils, as it often fails to follow the fibrils to their usually faint ends and often identifies the undisturbed fragments of a fibril (lying, e.g., between locations at which the fibril crosses other structures) as complete, separate fibrils. The lifetimes of spicules appear to lie in between those we obtain without considering SCFs to survive gaps and those obtained after interpolating across such gaps.

Such a similarity in some properties does not imply that SCFs and spicules both occur in similar magnetic structures. First, spicules are clearly identified only at some distance from the limb, i.e., at a much greater height than the SCFs, which are clearly located in the low chromosphere. Second, whereas spicules are more or less outward directed, as clearly shown by limb observations, the SCFs we see are well visible on the disk over a distance of up to 10^4 km, which implies that they are nearly horizontal. This conclusion is supported by the comparison carried out by Jafarzadeh et al. (2017b) between the SCFs imaged by SUFI and the magnetic field extrapolated into the chromosphere on the basis of a magnetostatic equilibrium (Wiegelmann et al. 2016). Jafarzadeh et al. (2017b) found that the azimuthal directions of both agreed very well, that the magnetic field lines corresponding most closely to the fibrils remained nearly horizontal. These field lines also mostly returned to the solar surface, thus forming very flat, low-lying magnetic loops. However, there are also (shorter) fibrils that are associated with field lines that reach up into the corona. These may be more closely related to spicules.

Also, we find that brightenings in around 50% of the SCFs start in the body of the fibril, rather than at its edge. These features are obviously not driven from one footpoint, as are jet-like structures such as spicules. For another ≈25% of the SCFs,

the brightness variation is similar to that presented in Figure 11, with the two edge-points of the SCF being brighter than the central part, which is also not compatible with a jet-like structure, where only one end of the structure is rooted in the photosphere, from where it points toward the upper layers of the atmosphere. All this suggests that our SCFs are more likely to outline small, loop-like structures, an interpretation which is also supported by the analysis of the curvature computed in Section 4.4. The brightness enhancement at both ends of the SCFs may be a result of a footpoint heating process, although the structure may simply reflect the fact that the broad Ca filter of SUFI allows the photospheric bright points to shine through. This is very similar to the structures seen by Pietarila et al. (2009), who also found many of their narrow fibrils to be rooted in underlying bright points.

The radiation transmitted through the SUFI 1.1 Å Ca II H filter comes from either the photosphere, or the lower chromosphere (average height of 600–700 km). This is very close to the limit of the small-scale canopies created by the granulation (Wedemeyer-Böhm et al. 2008), which are also found by Jafarzadeh et al. (2017b) on the basis of the magnetohydrodynamic-simulation assisted Stokes inversion output of Riethmüller et al. (2016). Some of the shorter SCFs may indeed be associated with the small-scale granular canopies, with possible similarities to the seething horizontal magnetic fields described in Harvey et al. (2007), or the horizontal fields detected by *Hinode* (Lites et al. 2008) and SUNRISE (Danilovic et al. 2010b). However, the longer SCFs are likely more closely related to the larger-scale canopy found over the network by Jones & Giovanelli (1982) and modeled by Solanki & Steiner (1990). Such extended horizontal field lines were found lying nearly parallel to the SCFs in the magnetostatic equilibrium computed by Wiegelmann et al. (2016).

The German contribution to SUNRISE and its reflight was funded by the Max Planck Foundation, the Strategic Innovations Fund of the President of the Max Planck Society (MPG), the Deutsche Zentrum für Luft- und Raumfahrt (DLR), and private donations by supporting members of the Max Planck Society, which is gratefully acknowledged. The Spanish contribution was funded by the Ministerio de Economía y Competitividad under Projects ESP2013-47349-C6 and ESP2014-56169-C6, partially using European FEDER funds. The HAO contribution was partly funded through NASA grant number NNX13AE95G. This work was partly supported by the BK21 plus program through the National Research Foundation (NRF) funded by the Ministry of Education of Korea. S.J. receives support from the Research Council of Norway.

References

Barthol, P., Gandorfer, A., Solanki, S. K., et al. 2011, SoPh, 268, 1
Berkefeld, T., Schmidt, W., Soltau, D., et al. 2011, SoPh, 268, 103
Danilovic, S., Beeck, B., Pietarila, A., et al. 2010a, ApJL, 723, L149
Danilovic, S., Beeck, B., Pietarila, A., et al. 2010b, ApJL, 723, L149
Danilovic, S., Hirzberger, J., Riethmüller, T. L., et al. 2014, ApJ, 784, 20
de Pontieu, B., McIntosh, S., Hansteen, V. H., et al. 2007, PASJ, 59, S655
Gafeira, R., Jafarzadeh, S., Solanki, S. K., et al. 2017, ApJS, 229, 7
Gandorfer, A., Grauf, B., Barthol, P., et al. 2011, SoPh, 268, 35
Gold, T. 1964, NASSP, 50, 389
Harvey, J. W., Branston, D., Henney, C. J., et al. 2007, ApJL, 659, L177
Jafarzadeh, S., Solanki, S. K., Stangalini, M., Steiner, O., et al. 2017a, ApJS, 229, 10
Jafarzadeh, S., Rutten, R. J., Solanki, S. K., Wiegelmann, T., et al. 2017b, ApJS, 11
Jafarzadeh, S., Solanki, S. K., Gafeira, R., van Noort, M., et al. 2017c, ApJS, 229, 9
Jones, H. P., & Giovanelli, R. G. 1982, SoPh, 79, 247
Lites, B. W., Kubo, M., Socas-Navarro, H., et al. 2008, ApJ, 672, 1237
Martínez Pillet, V., Del Toro Iniesta, J. C., Álvarez-Herrero, A., et al. 2011, SoPh, 268, 57
Parker, E. N. 1972, ApJ, 174, 499
Pereira, T. M. D., De Pontieu, B., & Carlsson, M. 2012, ApJ, 759, 18
Pietarila, A., Hirzberger, J., Zakharov, V., & Solanki, S. K. 2009, A&A, 502, 647
Pizer, S. M., Amburn, E. P., Austin, J. D., et al. 1987, Adaptive histogram equalization and its variations
Riethmüller, T. L., Solanki, S. K., Barthol, P., Gandorfer, A., et al. 2017, ApJS, 229, 16
Solanki, S. K., Barthol, P., Danilovic, S., et al. 2010, ApJL, 723, L127
Solanki, S. K., Riethmüller, T. L., Barthol, P., et al. 2016, ApJS, 229, 2
Solanki, S. K., & Steiner, O. 1990, A&A, 234, 519
van Ballegooijen, A. A., Asgari-Targhi, M., Cranmer, S. R., & DeLuca, E. E. 2011, ApJ, 736, 3
van Noort, M., van Der Voort, L. R., & Löfdahl, M. G. 2005, SoPh, 228, 191
Wedemeyer-Böhm, S., Lagg, A., & Nordlund, A. 2008, SSRv, 144, 317
Wiegelmann, T., Neukirch, T., Nickeler, D. H., et al. 2017, ApJS, 229, 18
Wiegelmann, T., Solanki, S. K., Borrero, J. M., et al. 2010, ApJL, 723, L185
Wöger, F., Wedemeyer-Böhm, S., Uitenbroek, H., & Rimmele, T. R. 2009, ApJ, 706, 148

The Astrophysical Journal Supplement Series, 230:11 (1pp), 2017 May https://doi.org/10.3847/1538-4365/aa6d71

Erratum: Morphological Properties of Slender CaII H Fibrils Observed by SUNRISE II (ApJS 229, 1, 6)

R. Gafeira[1], A. Lagg[1], S. K. Solanki[1,2], S. Jafarzadeh[3], M. van Noort[1], P. Barthol[1], J. Blanco Rodríguez[4], J. C. del Toro Iniesta[5], A. Gandorfer[1], L. Gizon[1,6], J. Hirzberger[1], M. Knölker[7,9], D. Orozco Suárez[5], T. L. Riethmüller[1], and W. Schmidt[8]
[1] Max Planck Institute for Solar System Research, Justus-von-Liebig-Weg 3, D-37077 Göttingen, Germany
[2] School of Space Research, Kyung Hee University, Yongin, Gyeonggi 446-701, Republic of Korea
[3] Institute of Theoretical Astrophysics, University of Oslo, P.O. Box 1029 Blindern, NO-0315 Oslo, Norway
[4] Grupo de Astronomía y Ciencias del Espacio, University of Valencia, P.O. Box 22085, E-46980 Paterna, Valencia, Spain
[5] Instituto de Astrofísica de Andalucía (CSIC), Apartado de Correos 3004, E-18080 Granada, Spain
[6] Institut für Astrophysik, Georg-August-Universität Göttingen, Friedrich-Hund-Platz 1, D-37077 Göttingen, Germany
[7] High Altitude Observatory, National Center for Atmospheric Research, P.O. Box 3000, Boulder, CO 80307-3000, USA
[8] Kiepenheuer-Institut für Sonnenphysik, Schöneckstr. 6, D-79104 Freiburg, Germany
Received 2017 April 12; published 2017 May 24

Due to a press error, in the original article an incorrect version of Figure 10 was published. IOP sincerely regrets the error and has reproduced the correct figure below.

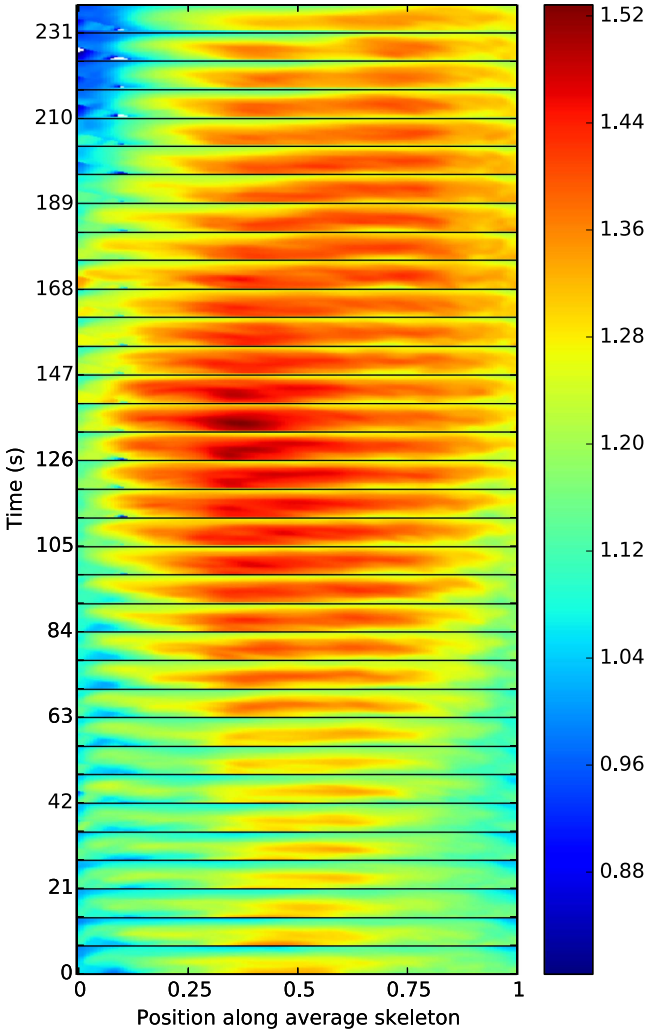

Figure 10. Temporal evolution of a SCF with a central brightening. The stacked images show the straightened fibril, with the backbone parallel to the *x*-axis in the center of each bin, surrounded by a $\pm 0\farcs3$ wide area covering the fibril. The individual images, recorded every 7 s, are separated by horizontal black lines. The length of the reference backbone of this fibril is 1620 km.

[9] The National Center for Atmospheric Research is sponsored by the National Science Foundation.